The 2022 Tonga Volcanic Tsunami: Lessons from a Global Event

Adam T. Devlin[1,2,3,4], David A. Jay[5], Stefan Talke[6], Jiayi Pan[1,4,7,*]

5 [1]School of Geography and Environment, Jiangxi Normal University; Nanchang, Jiangxi, China

[2]Cooperative Institute for Marine and Atmospheric Research, School of Ocean and Earth Science and Technology, University of Hawaiʻi at Mānoa; Honolulu, HI, United States of America

[3]Department of Oceanography, University of Hawaiʻi at Mānoa; Honolulu, HI, United States of America

[4]Institute of Space and Earth Information Science, Chinese University of Hong Kong; Shatin, Hong Kong, China

10 [5]Department of Civil and Environmental Engineering, Portland State University; Portland, OR, United States of America

[6]Department of Civil and Environmental Engineering, California Polytechnic State University; San Luis Obispo, CA, United States of America

[7]Key Laboratory of Poyang Lake Wetland and Watershed Research of Ministry of Education; Nanchang, China

[*]*Correspondence to*: Jiayi Pan (panj@cuhk.edu.hk)

15

Abstract The January 15, 2022, Tonga eruption provides a rare opportunity to understand global tsunami impacts of explosive volcanism, including "air-shock" tsunamis induced by Lamb waves travelling in the atmosphere, and to evaluate future hazards. The propagation of the air-shock and oceanic tsunami components were analyzed using globally distributed 1-min measurements of air pressure and water level (tide gauges and deep-water buoys). Oceanic tsunamis (up to 1.7m)
20 propagated primarily throughout the Pacific, but air-shock tsunamis arrived first and traveled globally, producing water-level perturbations in the Indian Ocean, the Mediterranean, and the Caribbean. The air-shock induced water level response of most Pacific Rim gauges was amplified, likely related to bathymetric processes. The air-shock wave repeatedly boosted tsunami wave energy as it circled the planet several times. In some locations, the air-shock was amplified as much as 35X relative to inverse barometer by Proudman resonance and topographic effects. Thus, a large volcanic air-shock (10-30mb) could cause a
25 3.5-10m near-field tsunami that would occur in advance of (usually) larger oceanic tsunami waves, posing an additional hazard to local populations. Present tsunami warning systems do not consider this threat.

30

1. Introduction

The immense energy of the Tonga-Hunga-Ha'apai volcanic eruption (20.54°S, 175.38°W) at 0415 UTC on 15 January 2022 ("the *Tonga Event*") rated a 5 on the Volcanic Explosivity Index (VEI), perturbed the atmosphere up to 35-55 km and was one of the strongest eruptions of the past 30 years (Witze, 2022). It produced a variety of atmospheric waves
35   from the surface to the ionosphere, the most relevant being Lamb waves that travelled the globe multiple times (Adam, 2022). Lamb waves (Lamb, 1911) travel with a celerity V ~300 ms^{-1}, which is faster than long gravity wave speed, except in the deepest parts of the ocean. We will refer to these Lamb waves as "air-shock waves," which then generated "air-shock tsunamis" at locations globally. Behind the (surface-trapped) Lamb waves, there were atmospheric gravity waves traveling at 200-220 ms^{-1}, about the speed of long waves in the deep ocean. Recent work has confirmed the presence of a slower
40   horizontal phase speed internal Perkeris wave (Perkeris, 1937; 1939) which has provided a resolution of long-standing issues about atmospheric resonance (Watanabe et al., 2022). In the ocean, a wave of depression caused by mass conservation drove the oceanic tsunami in the Pacific Ocean (Kubota et al., 2022). In this contribution, we investigate whether the characteristics and magnitude of atmospheric gravity waves can be isolated from the oceanic component. In principle, the characteristics and magnitude of the atmospheric gravity waves could be isolated at tide gauges and in ocean bottom pressure after the
45   arrival of the air-shock tsunami and just before the oceanic component. In practice, however, we observe a delay (~1-2 hours) of the water level response to the air-shock wave at the coast, and there is no clear way to identify the influence of atmospheric gravity waves.

The "Tonga-Tsunami" (with both oceanic and air-shock components) produced far-field water-level perturbations comparable to those from the 2004 Sumatran (Titov et al., 2005), the 2010 Chilean (Rabinovich et al., 2013), and the 2011
50   Tohoku Events (Mori et al., 2011). It spread throughout the Pacific Ocean and was measured in all ocean basins except the Arctic. We document here how the air-shock tsunami arrived before the oceanic component, ahead of tsunami forecasts (where they were available) and occurred in areas where the tsunami of seismic origin was absent. The Tonga Event was the most powerful since Mount Pinatubo in 1991 but was considerably less powerful than the 1883 Krakatoa eruption and several other geologically "recent" events (https://volcano.si.edu/search_eruption.cfm). What is the amplification potential of
55   these waves, as observed by the unprecedented number of gauges now available? Could a more significant volcanic event, such as a VEI 6 or 7 eruption, cause an air-shock tsunami of dangerous proportions ahead of forecasted arrival times, and in areas not reached by oceanic tsunami waves?

The global extent and rare nature of the Tonga event provides a unique opportunity to investigate the dynamics and impacts of a volcanic tsunami, especially the air-shock component. The worldwide network of high-frequency, real-time
60   water level (WL) stations is much more developed today than 10-15 years ago in the wake of the Sumatra and Tohoku tsunamis, allowing for detailed study of how sensitive different locations and geometries are to volcanically induced atmospheric perturbations. Though severe devastation during the Tonga Event was confined to the immediate vicinity

(mainly at other Tongan islands), most Pacific observation systems remained operational. Using these records, we assess the global spatial and temporal patterns of the tsunami and show that significant WL variations were produced in distant

65   locations, primarily due to the air-shock tsunami. Our investigation of 308 tide gauges (where the tsunami could be detected; though nearly 1000 locations were initially screened), 30 deep-water buoys, and 137 air pressure stations shows a patchwork of amplification, with some locations highly susceptible to air shocks and others relatively insensitive. In the Pacific, the air-shock and oceanic tsunamis occurred nearly sequentially and produced observable perturbations in water levels for more than three days after the eruption. These patterns demonstrate that volcanic tsunamis differ from seismic, landslide induced,

70   and meteo-tsunamis and provide crucial context for risk assessment and planning for future tsunamis stemming from large volcanic eruptions.

2. Physics of atmospheric tsunamis

Tsunamis of volcanic origin are uncommon; less than 150 have been documented (Levin and Nosov, 2009), and aside from a few large events like Krakatoa (Wharton, 1888), most have only local or regional footprints. Volcanic tsunamis

75   are usually induced by when magma rapidly displaces water, and large, rapid eruptions such as the Tonga Event can drive a planet-circling atmospheric shockwave that induces an air-shock tsunami. Volcanic activity is not, however, the only source of atmospheric tsunamis – local atmospheric disturbances can cause "meteo-tsunamis", independent of seismic or volcanic activity (Press, 1956; Šepić et al., 2014; Šepić et al, 2015; Olabarrieta et al., 2017). Meteo-tsunamis may have amplitudes up to 3-5m and cause significant coastal damage, but meteo-tsunamis are local events dependent on specific atmospheric

80   conditions and compatible undersea topography. The different source and dynamics of air-shock tsunamis made the manifestations of the Tonga Event global.

Air-shock and meteo-tsunamis share related ocean physics. Air-shock tsunamis are generated by Lamb waves from atmospheric explosions like Krakatoa or the Tonga Event that move, in this case, at ~1115km hr^{-1} (see Methods and Appendix A), while meteo-tsunamis are driven by strong, but slower weather disturbances (Šepić et al, 2015). Their

85   differences can be explained in terms of Froude number, F_A:

$$F_A = \frac{V}{\sqrt{gH}} \tag{1}$$

where: V is the atmospheric disturbance speed, H is water depth, and g is gravitational acceleration. For an air-shock, $F_A > 1$ for almost the entire ocean, while resonant, near-critical, conditions ($F_A \sim 1$) occur at moderate ocean depths for meteo-tsunamis.

90   Atmospheric forcing of tsunamis has been analyzed in linear (Garret, 1976) and more realistic nonlinear contexts (Pelinovsky et al., 2001). In either case, the solution consists of a forced ocean wave moving with the atmospheric disturbance, plus forward and backward free waves. Shallow water, linear free waves of small amplitude have celerity $c \approx \sqrt{gH}$, while nonlinear theory, relevant for $F_A \geq 1$, yields dispersive waves. The forced wave has amplitude proportional to $\frac{V^2}{V^2-c^2}\Delta P_A$ (13), with a "nominal amplification" relative to an inverse barometer effect of $a_n = \frac{V^2}{V^2-c^2}$; ΔP_A is the P_A (air

95   pressure) disturbance; $a_n > 1$ for most of the open ocean. When $F_A \sim 1$, the forced and forward-moving free waves coalesce, and the atmosphere feeds energy into the ocean (Proudman resonance), allowing waves to grow linearly with fetch (Williams et al., 2021). The actual forced wave "amplification factor," α, observed at an ocean bottom pressure gauge depends on many factors and may differ from a_n.

For a subcritical wave, a *rise* in P_A of 1mb causes a *fall* in WL of 10mm via the inverse barometer effect. But air-

100   shock forced waves are supercritical in ocean depths <9.7km, and the Bernoulli effect causes a *positive P_A* spike to drive a forced ocean wave as a *rise* in WL (Garret, 1976) with Proudman resonance occurring only in the deepest ocean waters. Amplification disappears ($a_n \cong 1$) in shallow water, but interaction of the forced wave with the continental slope and shelf will energize the free waves, allowing shallow-water amplification (Garret, 1976). An air-shock tsunami differs from a meteo-tsunami in that strong amplification is limited to deep ocean trenches, where fetch is limited, compensated by a

105   potential for ΔP_A to be much larger than for a meteo-tsunami. We define the overall amplification of a tsunami at a tide gauge, encompassing Proudman resonance and local effects, β.

What happens when a forced air-shock wave encounters a sudden change in depth? A depth change, from deep to shallow, requires the forced wave amplification, a_n, to decrease towards unity because $V^2 \gg c^2$ on the shallow side, spawning transmitted and reflected waves. The transmission and reflection coefficients that correspond to a_n, T and R

110   respectively, are given for a transition from h_1 (deep) to h_2 (shallow) by (Garret, 1976):

$$R[V, c_1, c_2] = \frac{V^2(c_1 - c_2)}{(V + c_2)(V^2 - c_1^2)}$$

$$T[V, c_1, c_2] = \frac{V^2(c_1 - c_2)}{(V - c_1)(V^2 - c_{12}^2)}$$

$$c_{1i} = \sqrt{gh_i}, i = 1,2 \tag{2a,b,c}$$

For a transition from h_2 (shallow) to h_1 (deep), the corresponding reflection and transmission coefficients are (Garret, 1976):

115

$$R^*[V, c_1, c_2] = R[V, c_2, c_1]$$

$$T^*[V, c_1, c_2] = T[V, c_2, c_1] \tag{3a,b}$$

The values in (2) and (3) apply, in principle, at the intersection of two infinite half-planes of depth h_1 and h_2, and only for a wave ray normal to the intersection of the half planes, though (Garret, 1976) shows that the above is a special case of the more general oblique incidence case. More practically, the depth transition must be abrupt, i.e., take place over considerably

120   less than one wavelength of the forced wave. For periods of ~10-60 minutes, that wavelength is ~180-1100km. Further, taking the ratios $\frac{R^*}{R}$ and $\frac{T^*}{T}$, we see that both the reflected and transmitted waves are smaller for a forced wave propagating offshore from the coast than for such a wave propagating onshore toward the coast. The offshore-directed case is also different in that the forced wave must be small, because the shelf will typically be less than a wavelength wide and the fetch for its development is limited. Still the transmitted and forced waves continue offshore, and the reflected wave returning to

4

125   the coast is small. This suggests that air-shocks coming directly from Tonga and from the antipodes may generate quite different responses in some locations, depending on whether they arrive from offshore or from land.

What happens at sharp, but more complex features, like deep ocean trenches, is presumably something intermediate between the Proudman resonance case, where the forced wave amplification factor, a_n, adjusts as the wave propagates, and the fission of the forced wave into transmitted and reflected components, described by R and T. Also, the shallow-to-deep

130   case as a wave encounters a trench from seaward is different from the deep-to-shallow case on the landward side of the trench. In the latter case, the forced wave must lose energy as a_n decreases. There is no such necessity at the seaward edge of the trench, and the forced wave may grow. Also, at a trench near the coast, the depth difference will typically be larger on the landward side than on the seaward side driving a larger transmitted wave. The transmitted wave may also grow over a continental shelf landward of the trench as $h^{-\frac{1}{4}}$, per Green's law (Green, 1838).

135   Other resonance processes may occur in specific circumstances. Pattiaratchi and Wijeratne (2015) cite quarterwave resonance and Greenspan resonance. The former is a standing wave resonance that can occur if the shelf width is ¼ of a wavelength of the forced wave. Greenspan resonance occurs when an edge wave propagating along a shelf meets a specific resonance criterion. Both of these processes have rather specific geometric requirements, and the high speed of air-shock waves renders both of them less likely for an air-shock tsunami than for meteo-tsunamis. Finally, the propagation of the air-

140   shock wave may also be influenced by atmospheric temperature gradients (Amores et al., 2022).

3. Methods

3.1 Data Inventory

We employ high-frequency (1-min) water level (WL) data from multiple worldwide data sources, including coastal

145   tide gauges and deep-water pressure buoys (see Appendix A for detailed procedures and uncertainty estimates). Air pressure (P_A) data at a variety of temporal resolutions (1, 6, and 10 min) is also acquired from multiple sources. Some regions, such as the European Atlantic coast, the East China Sea, and the Arctic Ocean did not show any tsunami-like WL fluctuations. In addition, some locations (e.g., Spain) that might have registered a tsunami lacked data during the relevant period. The buoys provide 1-min data during "active" WL events and 15-min data otherwise. However, many were not triggered until the air-

150   shock was past; thus, the air shock wave was often not captured, though the oceanic signal was clearly observed. In total, data from 308 tide gauges (out of ~1000 investigated) and 30 (out of ~60) deep-water buoys are employed, with 210 locations in the Pacific, and 98 in the rest of the world. Metadata for all tide gauges and deep-water buoys analyzed in this study (latitude, longitude, data source, and distance from the Tonga volcano) are given in Table S1, and metadata for air pressure stations are given in Table S2. We also list the tide gauges that were investigated but not analyzed in Table S3,

155   along with the reason for not using them, and show a color-coded map of the unanalyzed locations in Figure S1. We use detrended residual WLs to quantify the amplitudes of the largest positive and negative tsunami wave amplitudes at all stations from January 14 to 20, 2022. We also apply an EEMD analysis (Huang et al., 1998) to all WL and P_A data to remove

low frequency components and biases in mean water level to yield data in which the tsunami-related signals are dominant.

160   ### 3.2 Water Level (WL) Analysis

Air-shock magnitudes and arrival times, and the amplitudes of the largest positive and negative tsunami waves at each location are determined from the WL residuals via numerical and visual estimation of the residual time series (see Appendix A for details of calculations and a discussion of inherent uncertainty in this study). We compare the distances and first arrival times at all tide gauges stations via robust regression (Holland and Welsch, 1977) and find an estimate of the air-

165   shock velocity from the slope of the regression as 1054 ± 7 km hr^{-1} (Figure S2(b)), slightly less than that estimated from the air pressure gauges (1115 ± 3 km hr^{-1}; Figure S2(a)). These estimates can be compared to the much slower celerity estimate for the water wave component of the tsunami (708 ± 8 km hr^{-1}; Figure S2(c)), clearly demonstrating that the "first arrival" WLs are due to the air-shock. Note that the water-wave celerity corresponds to an average water depth of about 5km. MATLAB continuous wavelet transform (CWT; Rioul and Vetterli, 1991; Torrence and Compo, 1998; Lilly, 2017) routines are applied

170   to the WL and P_A residuals to confirm approximate arrival times (accurate within half a filter length) and to investigate the frequency response at each location. These are discussed for selected locations. P_A data (onshore and offshore) are compared with WL variability to investigate the relative synchronization of the P_A-spikes and associated WL variability. This is performed at certain Pacific locations, as well as in the entire Caribbean and Mediterranean Sea regions, where observed WL variations are solely due to atmospheric effects. We also generate multiple animations to show the tsunami propagation

175   globally and regionally. We animate 1-min global WLs taken between 15 and 18 January (Movie S1), and also animate the maximum WL reached in each hour surrounding the time shown in the frame (i.e., ±30 min) in Movie S2. Regional animations for the Caribbean (Movie S3) and Mediterranean (Movie S4) are also provided. For these, we show both the WL and PA residuals in separate panels. The Caribbean animation runs from 15 to 19 January since the air-shock effects were longer-lasting there.

180

3.3 Energy Decay Analysis and β factor calculations

We calculate the energy decay of the Tonga event and compare to other recent tsunamis. Following Rabinovich, (1997) and Rabinovich et al (2013), we detide 1-min NOAA WL data, remove any residual trend, and then produce power spectra for 6hr segments of the WL residual, with an overlap of 3 hours between successive analyses. A multi-tapered

185   method (McCoy et al., 1998) was applied, because it reduces noise and edge effects, but still conserves energy. The energy within the tsunami band (between 10 minutes and 3 hours) was then integrated for each 6hr period and an exponential decay model of form $E = E_o e^{\frac{-t}{t_d}}$ applied, where E_o is the peak energy in the fit and t_d is the e-folding (decay) time scale.

We use P_A-spike and air-shock induced WL-fluctuation amplitudes to estimate β at locations where the air-shock was clearly observed and where co-located or nearby P_A records were available. β is calculated as the ratio of the maximum

190   (positive) residual WL at air-shock arrival divided by the maximum (positive) air pressure spike, with P_A converted to a WL

level fluctuation assuming the usual inverted barometer effect of 10mm WL change for 1mb P_A change. In total, we are able to calculate β at 231 locations. For the "first arrival" of the air-shock calculated, we only consider the first air-shock on 15 January, but for the β calculations, we use the largest WL amplitude closely following a P_A-spike visible in the record; for many locations in the Atlantic and Mediterranean, this occurred on the second or third pass of the atmospheric disturbance.

195 ## 4. Results

4.1. Tonga global tsunami impacts as determined from tide gauges

The Tonga Event produced an air-shock tsunami with a global footprint, along with an oceanic tsunami confined primarily to the Pacific (Figure 1). Water-level perturbations were recorded along the west coast of Africa, in the Mediterranean and Caribbean Seas, in the Indian Ocean, and elsewhere (Fig. 1(a),(c)). Tsunami arrival times at most places
200 closely correlate with arrival of the air-shock (Fig. 1(b),(d)), which propagated concentrically from the source around the planet, reconverging at the antipode. See also Tables S4-S6 and Figures S3-S12.
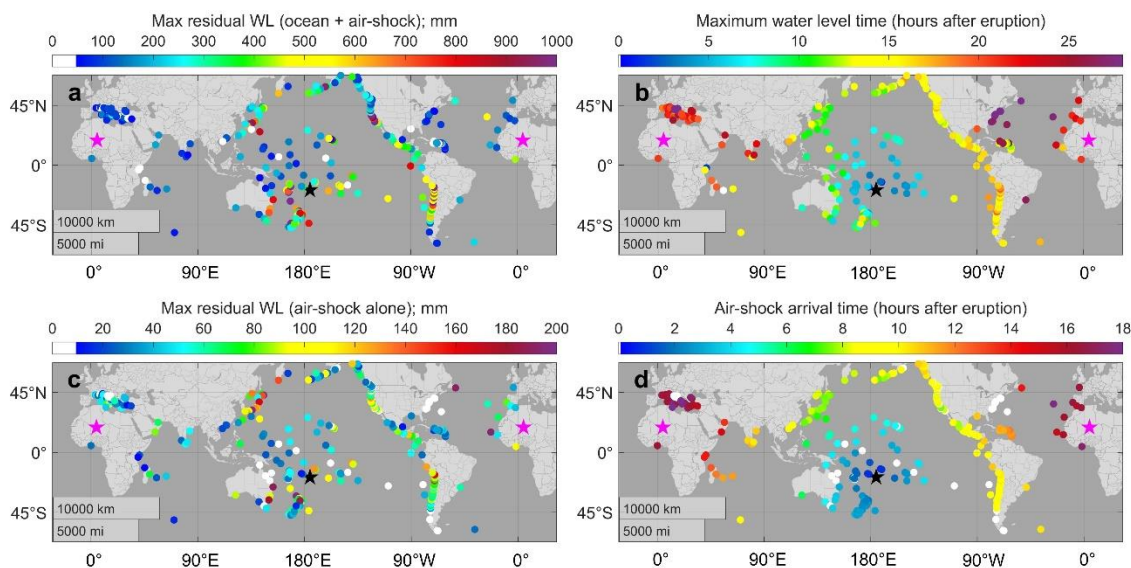

Figure 1. Tonga tsunami global manifestation: (a) maximum amplitude; (b) time of maximum amplitude; (c) air-shock amplitude; and (d) air-shock arrival time. White markers in (c) and (d) indicate locations where air-shock wave properties
205 could not be determined. The location of the eruption and its antipode are shown by black and magenta stars, respectively. Map backgrounds made in MATLAB using Natural Earth (naturalearthdata.com).

The largest amplitude far-field tsunamis occurred at dispersed Pacific Ocean locations, without a clear spatial decay pattern (Fig. 1(a),(b)). Several gauges within 3000 km of the eruption registered tsunamis >1m. Moderate tsunamis were

measured at most island locations. In Hawaii, only the gauge at Kahului measured waves >0.5 m; several islands in French
210 Polynesia also reached this level. Consistently stronger responses occurred around the periphery of the Pacific, with wave
heights of >1m at Kushimoto, Japan, four locations in Chile, four locations in California, and one in Alaska. Away from
Tonga, the largest maximum and minimum measured WLs in the Pacific occurred at Chañaral, Chile (+1.73m and -1.95m);
the largest in the US was Port San Luis, CA, at +1.34m. A ~2m tsunami was reported, but not measured, near Lima
(https://www.nytimes.com/2022/01/21/world/americas/peru-oil-spill-tonga-tsunami.html). Generally smaller amplitude
215 waves occurred in the Pacific Northwest, Alaska, and Central America.

The "first arrival" map (Fig. 1(c)) shows a circular pattern emanating outwards from Tonga. Robust regression
between the "first-arrival" times of the air-shock and the distances from Tonga yield a slope of 1115±3 km hr^{-1} (Figure S2),
not much less than sound speed at sea-level (1225 km hr^{-1}), and similar to the estimate of 1080-1170 km hr^{-1} for the Krakatoa
tsunami (Garret, 1976). The air-shock amplitudes are small (<0.1m) in most locations (Fig. 1(d)), moderate (up to 0.15m) at
220 certain locations in Chile, the Northeastern Pacific, Russia, and Hawai'i, and up to 0.22 m at some locations in Japan,
Australia, and New Zealand (Table S5). In the Pacific, this pattern can be contrasted with the less regular arrival times of the
largest amplitude oceanic tsunami (Fig. 1(b)) and the time difference between "first arrival" and high-water (Figure S9). The
latter emphasizes that the air-shock tsunami can occur many hours before the oceanic tsunami, where both were observed.
These results are confirmed by regression of WL "first arrival" times (i.e., from the air-shock) against tide gauge distance
225 from Tonga, and similarly for arrival times of the oceanic wave (Figure S2). The slopes give velocity estimates for the two
tsunami components: 1056±7 km hr^{-1} for the air-shock wave, and 708±8 km hr^{-1} for the oceanic wave, consistent with a
mean ocean depth of about 5km. The air-shock tsunami arrives at tide gauges after the air-shock itself because the waves
observed at tide gauges are subcritical, free waves.

Several Indian Ocean tide gauges (East Africa, Oman, Sri Lanka, and India) showed WL changes shortly after the
230 air-shock wave arrived, but little evidence of an oceanic tsunami. In the Atlantic Ocean there was a strong signal in Senegal,
Ghana, the Cabo Verde, Canary, and Azores Islands. The last of these showed a large WL amplitude (~0.6m), but this area is
undergoing volcanic activity with frequent seismicity. While no nearby air pressure record is available to confirm a
relationship to the air-shock here, no strong seismic activity was recorded either, so the causality of this result is uncertain.
These gauges are located within ~3000 km of the antipode of the Event (20.54° N, 4.62° E in the Sahara Desert), where the
235 concentric shock waves re-converge. The resulting interference pattern may have increased the magnitude of the air-shock
and subsequent tsunami.

In the Eastern North Atlantic, small tsunamis occurred after the second pass of the air-shock on 16 January, e.g., at
St. Johns, Canada (~0.2m). Storminess after 16 January precluded further detection there and in the Baltic Sea; and little or
no signal was seen on the European Atlantic Coast. Wide-spread air-shock tsunamis occurred in the Caribbean and

240 Mediterranean Seas, the latter being close to the antipodal point of the shockwave. In both regions, successive occurrences of the air-shock wave have different impacts on WL variability.

Global and regional animations of 1-min and hourly maximum WLs (Movies S1 and S2) depict the progression of the tsunami and the role of the atmospheric wave. Lower WLs from the air-shock tsunami are observed at most locations in advance of the larger oceanic tsunami. Regional animations for the Caribbean and Mediterranean (Movies S3 and S4), show

245 the WL and air pressure variations side-by-side. Following each air-shock, WLs "ring" for hours, only to be re-stimulated by the next pass of the air-shock. The movies also suggest that tsunami characteristics vary between closely spaced stations, because of local bathymetry, ambient currents, and the orientation relative to the source (Šepić et al., 2015; Garett, 1976; Williams et al., 2021). Air-shock properties change with atmospheric stratification and due to dispersion as the shock propagates; the directionality of the air-shock (towards or from land) also matters (Garett, 1976). Thus, the level of threat

250 from an air-shock event is locally variable, despite its global reach.

4.2. Tonga Pacific tsunami propagation as determined from deep water buoys

The network of National Data Buoy Center (NDBC) deep-water tsunami warning buoys provides significant spatial coverage of the Pacific and can reveal the offshore characteristics of strong oceanic signals like tsunamis (e.g., surface amplitude) without contamination by surface swell waves. These buoys generally provide a 15-min temporal resolution but,

255 when "triggered" by large signals, record 1-min data. We examined all available buoys but found that many buoys did not record any data at all during the Tonga event. We found 30 NDBC buoys in the Pacific which caught at least part of the tsunami (air-shock or oceanic); however, only a subset "caught" the air-shock tsunami (12 buoys). Locations are given in Figure 2(a) and details of the buoys are given in Table S1. Ten locations measured an air-shock tsunami in the Western Pacific, one in Alaska, one in Hawaii, and none in the Eastern Pacific. The Western Pacific data reveals a similar spike-like

260 waveform, with a steep rise followed by a rapid decrease. The magnitude of the air-shock WL response nearly consistent across the basin, except at two of the nearest buoys to Tonga (55015 and 51425), where amplitudes were 7.0 and 5.8 cm, respectively. All other air-shock magnitudes were between 2.5 and 4.0 cm, even at a great distance from Tonga (Figure 2(b)).

The energy generated by the Tonga tsunami may have been sustained by repeated returns of the atmospheric wave

265 at many locations. Can the spatial characteristics of energy decay be suggested from the limited buoy data? We next make an estimate of the "persistence" of the tsunami in the Pacific by determining the length of time (in hours) that the buoys were "triggered" for one-minute resolution observations. This metric, possibly influenced by instrumental problems at some locations, allows a simple, if imperfect, estimate of tsunami energy decay for individual buoys and for regional averages. The longest regional "persistence" was found in central region near Tonga, but this estimate is skewed by a few longer

270 results, e.g., 52406 recorded for 30 hr, far longer than any other location, in contrast to nearby buoys 52402 and 52404 (each

only about 5 hr); for reasons unknown. At the periphery of the basin, the regional persistence was 6.5 hours in the West, about 9.2 hours in both the Northeast and Northwest, 11.75 hours in the Pacific Northwest/California, and 12.33 hours around South America. Thus, we generally see a longer persistence time in the northwest/northeast/east Pacific then in the west/southwest (Figure 2(c)). The maximum air-shock magnitude (where detected) and the persistence times at all buoys are given in Table S7.

A sub-set of five buoys provide a good summary of air-shock tsunami behavior in deep water (Figure 2(d)). Two buoys (52402 and 21420) are almost exactly on a great circle with each other and the Tonga eruption; buoy 52402 is ~ 5000 km from Tonga, while 21420 is ~2700 km further towards the southern coast of Japan. These two buoys are plotted on the same axis in Figure 2(d); their responses are quite similar. The air-shock tsunami maximum WL at the first buoy is about 3.8 cm and is about 3.0 cm at the second; the subsequent WL oscillations at both buoys are also similar in form. This suggests that the air-shock response of the oceanic WL decayed very slowly, at least across the Pacific basin. The full set of WL responses at all buoys are given in the Supplement and compared by region (Figures S13-S18).
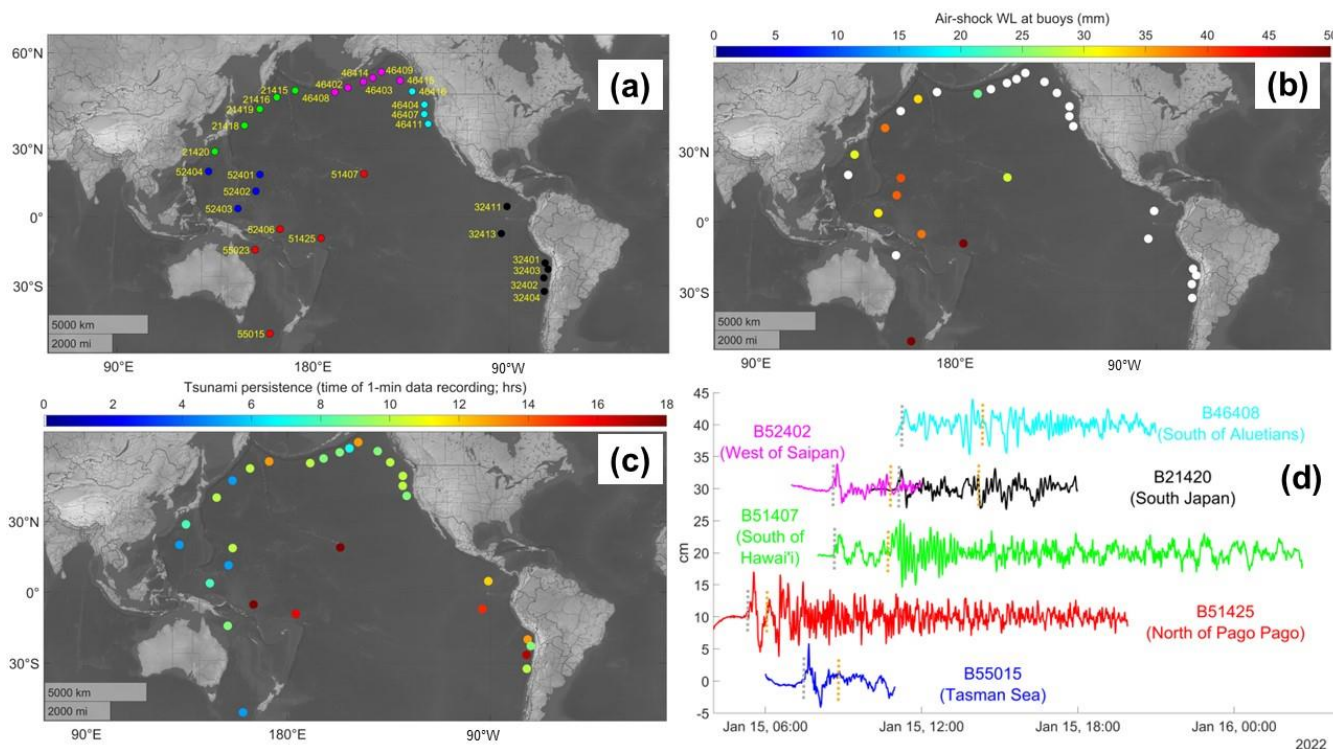

Figure 2 Pacific deep-water NDBC buoys used to detect the air-shock and oceanic tsunami of the Tonga event. (a) Buoy locations and NDBC buoy designation numbers, with colors used to show regional delineation (red: Central/Southwest; dark blue: West; green: Northwest; magenta: North; cyan: Northeast; black: Southeast). (b) Maximum air-shock-induced WL

10

(mm) detected at buoy according to color scale at top of map White markers indicated that the air-shock was not detected at the buoy. (c) Persistence time of the tsunami signal at each buoy, representing the length of time that each buoy recorded at 1-minute resolution (hr). (d) WL response to the air-shock and oceanic tsunami at six deep-water buoys in the Pacific. Each
290 buoy is offset 10 cm vertically from each other. Air-shock tsunami arrivals based on a theoretical travel time of 1115 km/hr^{-1} are indicated by grey vertical lines, and oceanic tsunami arrivals based on an average travel time of 700 km/hr^{-1} are indicated by orange vertical lines. Map backgrounds made in MATLAB using Natural Earth (naturalearthdata.com).

4.3 Coastal characteristics of air-shock tsunamis

295 As the air-shock tsunami propagates from deep water to the coast, we observe several cases in which an abrupt change in geometry produces a large amplification in the air-shock tsunami wave. We return to the example of buoys 52402 and 21420 discussed above, and now compare data from the buoy closer to Japan (21420) with the nearest coastal tidal gauge that also has P_A data, Kushimoto, Japan (Figure 3). The first air-shock of ~0.6 mb occurs at ~1130UT on 15 January at Kushimoto (Fig. 3(a),(c)). The WL response in the P_B record (a positive ~30mm spike then a ~30mm negative one) is
300 direct and presumably represents the forced wave. We compare the two closest P_A records to the P_B data (Aburatsu and Kushimoto; see Methods for details). Longwave celerity at buoy depth (5700m) is 850km hr^{-1}; $a_n = \frac{V^2}{V^2-c^2} \sim 2.4$, relative to the observed amplification of $\alpha \cong 4$. The CWT scaleogram in Fig. 3(e) shows the WL response to the air-shock at ~10hr post-eruption as two relatively distinct bands of energy with periods of ~1hr and 5-10min; these fade within ~1.5hr.

Kushimoto WLs effectively illustrate the potential for amplification of air-shock tsunamis. The first (air-shock)
305 waves arrived between 1200 and 1450UT (Figs. 3(b),(d)), prior to the oceanic tsunami at about 1450UT; their period is ~0.3hr (Fig. 3(f)); shorter-period energy is seen only after the arrival of the marine wave. The initial positive air-shock amplitude of ~210mm is a response to the air-shock and represents an amplification of ~7X relative to the forced wave, and β~35X relative to the air-shock, for which the inverse barometer response would be only 6mm. Apparently, the Japan trench with depths to 8km ($a_n \approx 5.5$), between buoy 21420 and Kushimoto allowed considerable growth of the forced wave
310 relative to Fig. 3(a),(c). A large volcanic explosion can cause an air-shock of 30-60mb (Schufelt, 1885), which could potentially drive a disastrous air-shock tsunami before the arrival of oceanic waves.
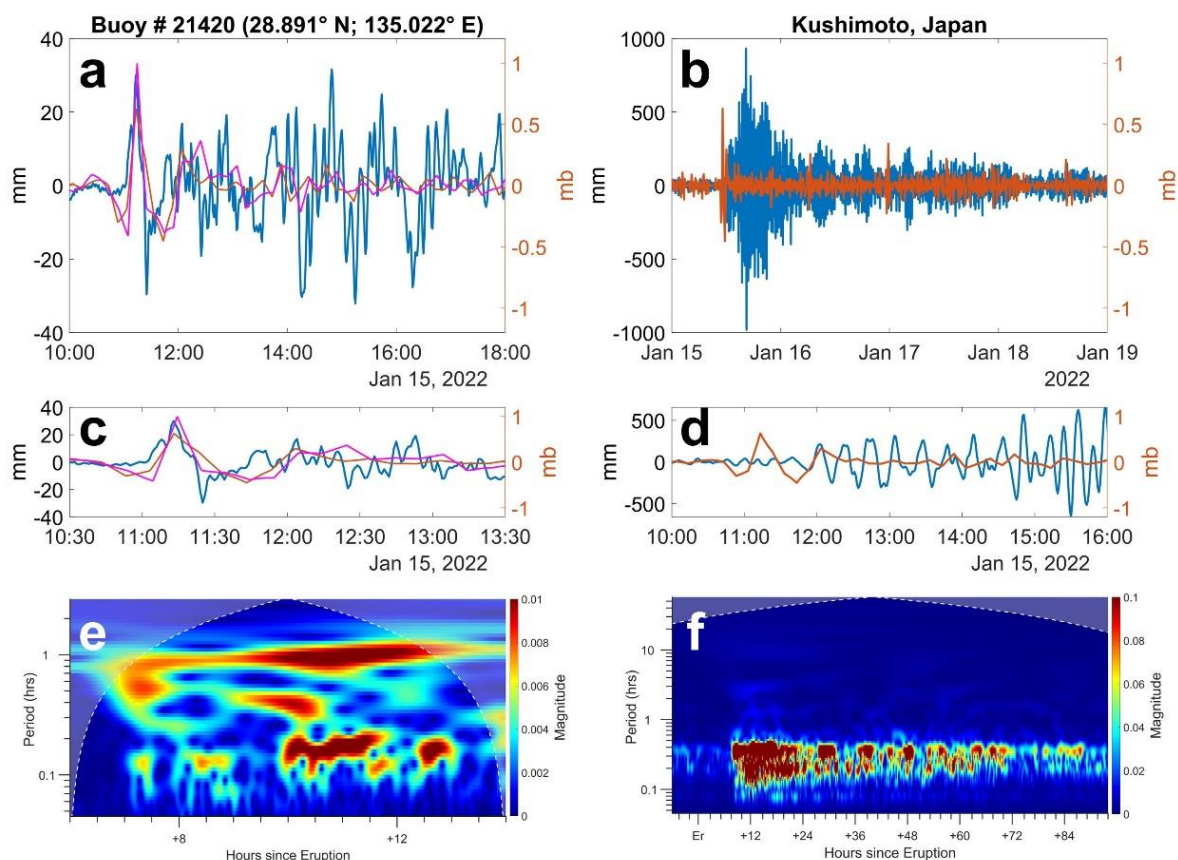
Figure 3. Tsunami response at NOAA P_B buoy 21420 and a coastal tide gauge (Kushimoto. Japan): (a) Residual P_A at
Kushimoto (orange) and Aburatsu (magenta), and detided residual buoy WL (blue) with P_A records shifted plot 26 and
16min to account for distance from the buoy (see Appendix A for details); (b) P_A (orange) and detided residual WL (blue) at
Kushimoto; (c) expanded view of (a) showing arrival of an air-shock tsunami as a supercritical forced wave at 1150UT,
ahead of the marine wave at 1450UT (c); (d) expanded view of (b) showing the arrival at Kushimoto of an air-shock tsunami
as a subcritical free wave at 1200UT; (e) buoy residual WL CWT scaleogram, 6-14hr post-eruption; (f) Kushimoto WL
CWT scaleogram for 92hr post-eruption.

Observations near Hilo show similar phenomena to those observed at Kushimoto (Figure 4). We use observations
from NOAA tsunami bottom-pressure (P_B) buoy 51407 in 4.7 km water depth south of Hilo combined with atmospheric-
pressure (P_A) and WL data from Hilo (NOAA station 1617760) to show how the signal evolves from offshore to coastal
waters. Fig. 4(a),(c) show P_A and P_B data (converted to WL). Despite the distance (~100 km) between the two records, the
WL and P_B responses are almost simultaneous, at 0854 UT. The first P_A pulse of ~1.5mb elicits an oceanic response of
~30mm (α~2) of the same sign, as expected for a super-critical wave and similar to the response at Kushimoto. This modest

12

amplification is still slightly larger than expected for $a_n \sim 1.2$. Smaller positive WL pulses follow the first; after the third, these pulses are overlain by the beginnings of the ocean tsunami signal at ~1030 UT. These may be a soliton train, as predicted by the nonlinear theory (Pelinovsky et al., 2001). The CWT scaleogram in Fig. 4(e) shows that ocean waves with

330   periods of 0.15-0.2hr arrived at buoy 51407 before 1100 UT; shorter waves (periods <0.1hr) arrived later, confirming the weakly dispersive character of the oceans waves. The air-shock tsunami is also clearly visible. It appears just before 0900 as a broad band signal with periods of 0.4-1.1 hr. Over time, the pulse shifts to higher frequencies and then disappears by ~1200 UT.

The Hilo detided residual WL data present quite a different appearance from the offshore P_B data (Fig. 4(b),(d)).
335   The first substantial deviation (~120mm) begins at 0928 UT (~1 hr after the P_A-spike) with a *negative* excursion rather than a *positive* one. This is followed by a series of smaller oscillations leading up to the arrival of the oceanic tsunami at about 1137 UT. The forced wave is not evident, and the early arriving air-shock tsunami waves at Hilo are likely free waves that have propagated around the inland on which Hilo sits and then amplified, having been generated at the abrupt rise of the island platform; the total amplification is β=9X. The waves from the ocean tsunami wave reach ~400mm, which represents an
340   amplification of about 5X relative to the same P_B waves at the buoy. Records from nearby Hawaiian gauges show similar features. The CWT scalogram for Hilo WL in Fig. 4(f) emphasizes the absence of longer period tsunami waves with periods around 1 hr. Instead, the weak air-shock wave response is followed by waves with similar periods, ~0.15 to 0.7 hrs. Over the next several days, the oscillations weaken, with the shortest period waves disappearing first. Hilo is well known to be resonant to tsunamis, and our observations may be related to quarterwave resonance (Pattiaratchi and Wijeratne, 2015).
345   However, a summary investigation of other tide gauges in Hawaii shows similar behavior as at Hilo.
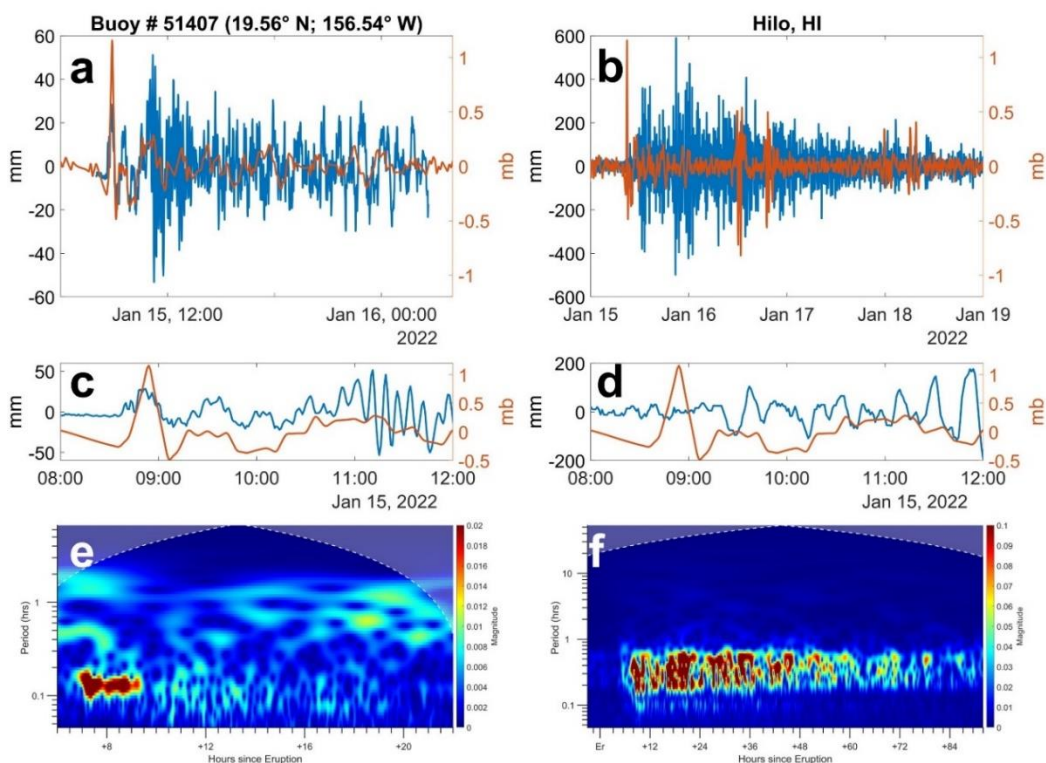
Figure 4. Comparison of WL (blue, mm) and P_A (orange, mb) at offshore buoy 51407 and Hilo, HI. (a) P_A at NOAA tide
gauge 1617760 Hilo, HI and detided WL residual from NOAA P_B Buoy 51407 south of Hawai'i following the Tonga Event;
(b) P_A and detided residual WL (blue) at Hilo; (c) expanded view of (a) showing the arrival of an air-shock tsunami at Buoy
350 51407 in the form of a supercritical forced wave at 0854 UT, ahead of the marine wave arrival at ~1054 UT (c); (d)
expanded view of (b) showing the arrival at Hilo of an air-shock tsunami in the form of a subcritical free wave at 0928 UT;
(e) a CWT scaleogram of buoy heights from P_B for hr 6-24 post-eruption; (f) a CWT scaleogram of WL measured at Hilo for
92hr post-eruption.

355   Kushimoto and Hilo are only two Pacific examples of air-shock effects. Air-shock magnitudes were similar to
Kushimoto at other Japanese locations and were 50-210 mm in New Zealand and Eastern Australia. Much smaller (~20 mm)
air-shocks were seen around Hong Kong. In the Eastern Pacific, distant from Tonga, air-shock waves arrived 3.5 (California)
to 5hr (Chile) before the oceanic tsunami, allowing their WL effects to be easily distinguished (Fig. 1(a),(c), Table S3), and
both regions had particularly high maximum tsunami amplitudes (±1.1-1.7m). Air pressure (P_A) spikes of ±0.6-0.7mb and
360 +1.5 and -0.8mb at Port San Luis, CA, and Coquimbo, Chile (Figure 5) led to air-shock tsunamis of +110 and -150mm,

14

respectively, with total amplifications of β~15-25X at Port San Luis (Fig. 5(c), and ~6X (positive wave) and 30-40X (negative wave) at Coquimbo (Fig. 5(d). There were at least six arrivals of the air-shock over 3d. This recurrence, coupled with very long decay times (below) caused WL disturbances to continue for >90hr, emphasizing the role of the air-shock in "recharging" the combined oceanic+air-shock tsunami (Fig. 5 (e-h)).
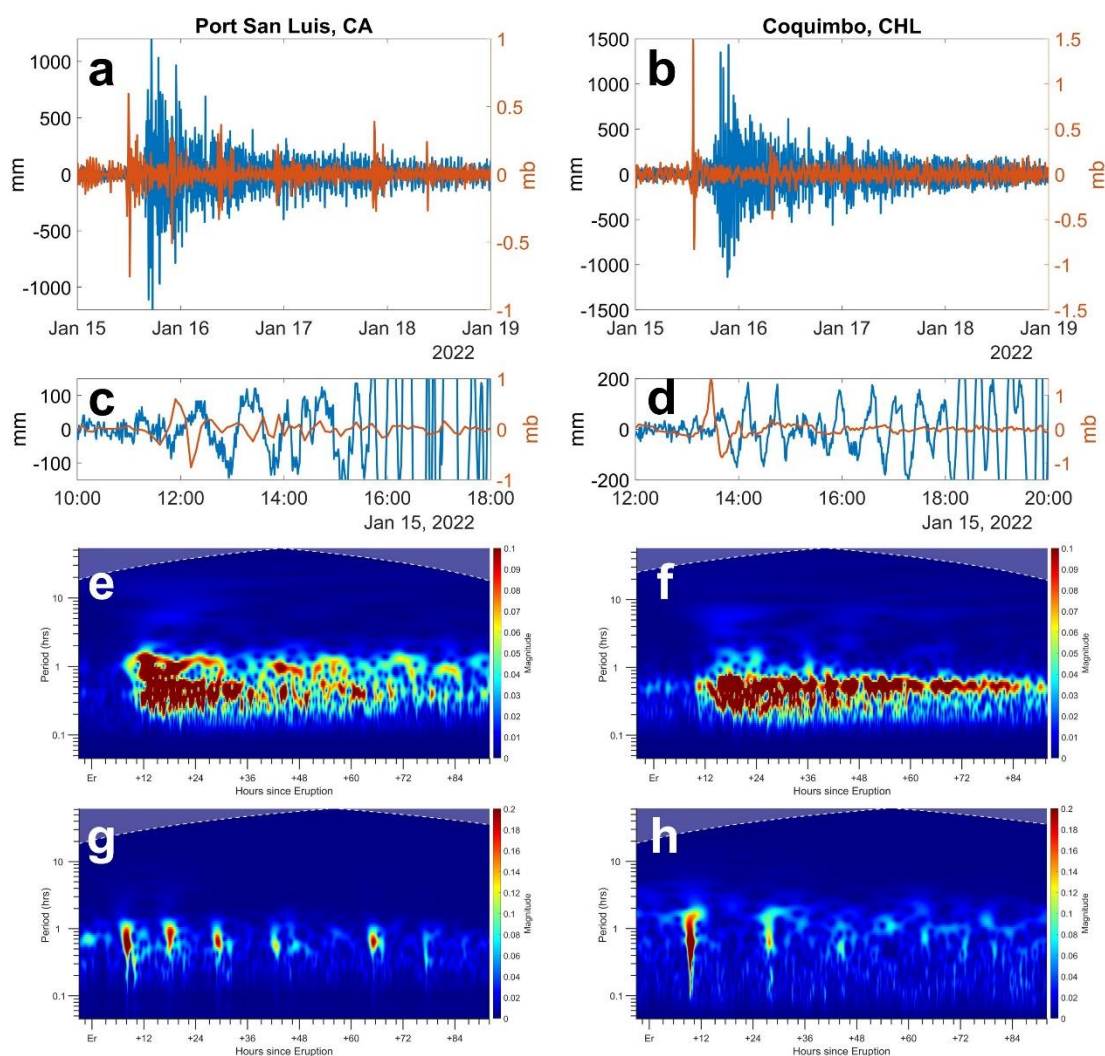

Figure 5. Residual WL (blue, mm) and detrended air pressure (orange, mb) at: (a) Port San Luis, California (NOAA Station 9412110) and (b) Coquimbo, Chile; (c) and (d) expanded views of the WL and P_A records for the period of the initial arrivals of the atmospheric and marine tsunami corresponding seen in (a) and (b); and scaleograms from CWT analyses of WL in (e) and (f) for P_A in (g) and (h).

365

15

370

       These Pacific examples demonstrate the combined oceanic and air-shock tsunamis; in other regions, the air-shock tsunami occurs in isolation. At Charlotte Amalie in the Caribbean (Figure 6), the P_A-spikes and resulting air-shock tsunamis are well correlated (Fig. 6(a)). The first P_A-spike of ~1.2mb led to waves of 80mm about an hour later, apparently from the free wave (Fig. 6(b)). In contrast, the third P_A-spike of ~0.5mb apparently excites a forced wave with amplitude of about

375   50mm, simultaneous with and of the same sign as the P_A-fluctuations (Fig. 6(c)). Waves arriving an hour later and presumably representing the free wave were larger, ~80mm, giving α = ~16. The fourth P_A-spike ~±0.2mb again excited a forced plus free wave response, with the later waves being as large at ±100mm (Fig. 6(d)). This corresponds to an impressively large β = ~30. The CWT scaleogram shows that water level in this harbor responds most strongly at periods of ~0.5 to 0.9hr (Fig. 6(e)). The CWT of P_A shows eight spikes at ~12hr intervals, suggesting that the air-shock circled the

380   planet at least four times (Fig. 6(f)). The largest WL response occurred from the fourth air-shock (Fig 6(e), (f)) for yet unknown reasons. Other gauges in the Caribbean showed significant air-shock effects (Figure S11) that were strongest on the second or third pass of the atmospheric disturbance. While β varies with the event, there are numerous volcanos in the Caribbean, and severe tsunamis (both air-shock and oceanic) could be a very real threat in locations where amplification occurs.
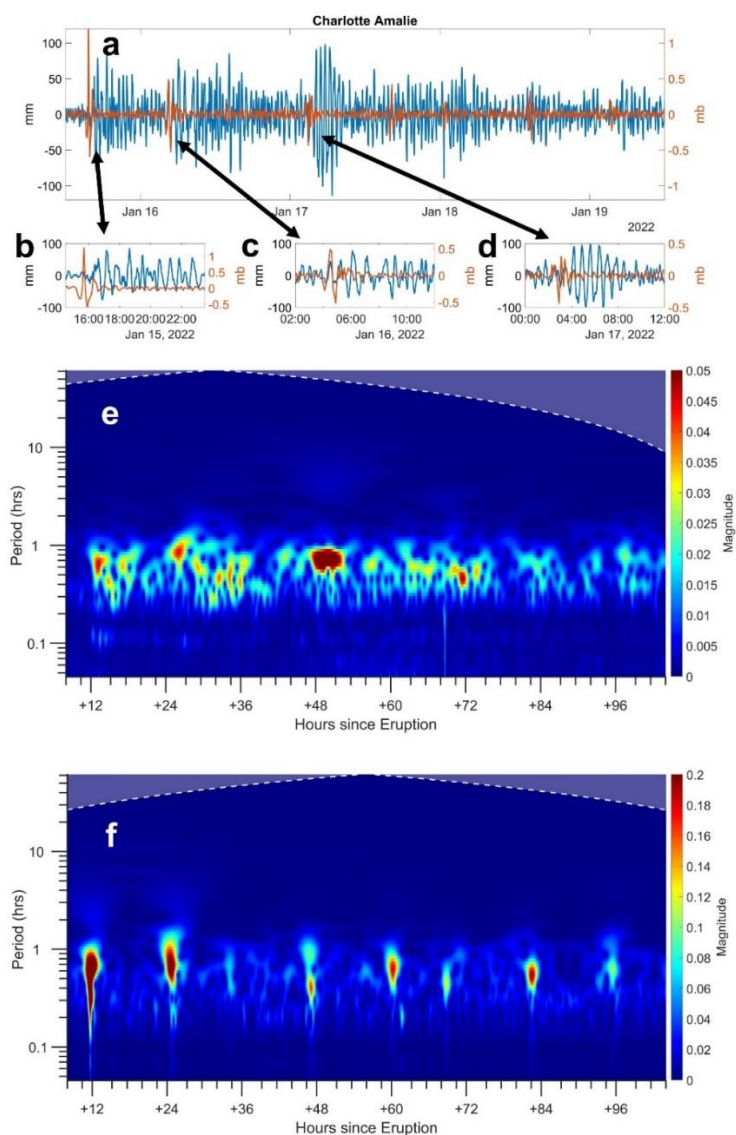
Figure 6. Air-shock tsunamis at Charlotte Amelie (NOAA gauge 9751639) in the Caribbean: (a) Residual WL variability (blue) and P_A (orange) from UT 15 to 19 January 2022; (b)-(d) expanded views of (a) at the times of the 1st, 2nd, and 4th P_A-spikes; (e) and (f) CWT scaleograms of the WL and P_A records in (a).

Air-shocks were generally smaller in the Mediterranean than in the Caribbean, perhaps because of the greater distance from Tonga and the complex land topography in the region. Still, air-shocks were measured at many locations, but largest in Sicily, Sardinia, and the "boot" of Italy. Because this region is close to the antipode, the first P_A waves arriving

17

from opposite directions were only a few hours apart, at ~ 2000 and 2330 UTC on 15 January, producing a "wave packet" rather than a clear P_A-spike. A weaker second packet occurs ~38hr later at ~1200 UTC on 16 January, followed by a third

395   packet at ~0000 UT on 19 January, not seen at all stations. WL records usually show a single, long-lasting event following the first P_A-packet arrival, with muted responses for the second and third packets. The largest tsunami amplitude, ~300mm (Figure S12), occurred at Crotone, Italy after a steady build-up from the air-shock arrival. At a small number of stations, e.g., Cagliari, Italy, there were air-shock tsunamis for multiple P_A-packets, as in the Caribbean (Figure S11). Finally, a few locations in the Adriatic Sea had no response to the first wave packet but responded strongly to the second air-shock, with β

400    $\approx$ 8 -13.

4.4. Energy decay

The Tonga event released significant energy and persisted longer in the Pacific than other recent tsunami events. Our estimate of energy E_o for the Tonga Event (0.0096m^2, N= 37) is comparable to the Chilean event (0.001m^2; N =28) and about 3.8x less than the Tohoku Event (0.036m^2; N=40). Previous estimates for the Chilean and Tohoku Events were 0.009

405   m^2 and 0.032m^2, respectively (Rabinovich et al., 2013). Decay time scales for the Tonga Event varied from 29-44hr (Alaska), 25.4hr (Santa Barbara) to 37hr (San Diego) on the US West Coast, and 22.2hr (Nawiliwili, Hawaii) to 29.3hr (Pago Pago, Samoa) for island stations (Figure S19). The Tonga decays are notably longer than other events, especially in Alaska and (most) California locations. The differing timescales depend on distance from the event, frequency content (high frequency decays more quickly), and shallow water processes (Rabinovich et al., 2013). Our estimated median t_d values for

410   the Tohoku, Chile and Tonga events are 26.6±2.4hr (N=40), 27.6±2.8hr (N=27) and 31.0±2.6hr (N=37), respectively (Figure 7). Previous estimates for the Tohoku and Chilean Events were 24.6 and 24.7hr. The longer decay time of Tonga emphasizes the importance of the air-shock, which "refreshed" the tsunami as it repeatedly circled the planet. The long energy decay scales calculated for the Northern Pacific are in line with our simple estimates of decay taken from the buoys; longest in the Northern/Northeast Pacific and near Tonga (e.g., Hawai'i and Pago Pago).
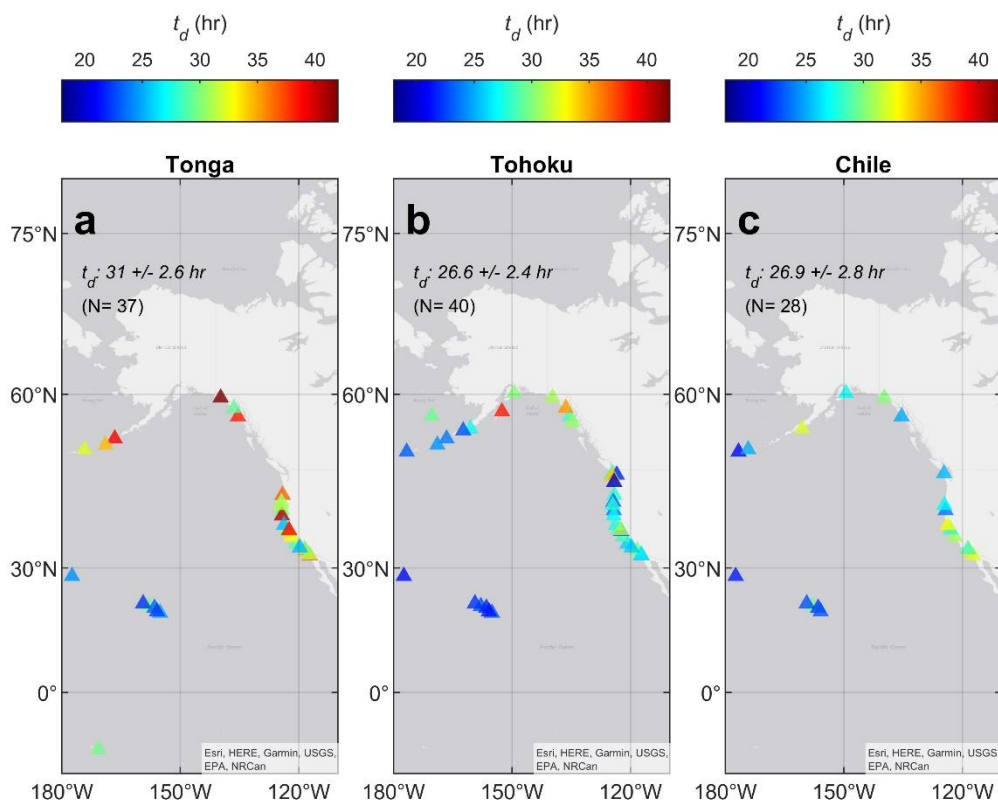
415

Figure 7. Decay timescales (hours) of recent tsunami events at NOAA gauges in the Northern Pacific; showing (a) Tonga; (b) Tohoku; and (c) Chile. Median t_d, errors, and number of stations used are given in each panel. Map backgrounds made in MATLAB using data hosted by Esri®.

420

4.5. Amplification, β

Amplification, β, is a vital indicator of future air-shock tsunami hazard. It was calculated for ~75% of all tide gauge locations where the air-shock was detected in a nearby P_A record (Tables S5 and S6). Clearly, β is highly local, with values of 15-35 at 26 stations in all regions where an air-shock tsunami was observed; over 40 locations had a $\beta > 10$ (Figure 8 (a-d)). The largest values of β are seen in Japan, the Northeast Pacific, New Zealand and Australia, and the Caribbean. Wherever high β values were observed near an active volcano, there is the potential for a large air-shock tsunami. Note that β values are uncertain by ~30% (see Appendix A), mainly due to the uncertainty of P_A observations with low amplitudes and coarse temporal resolution.
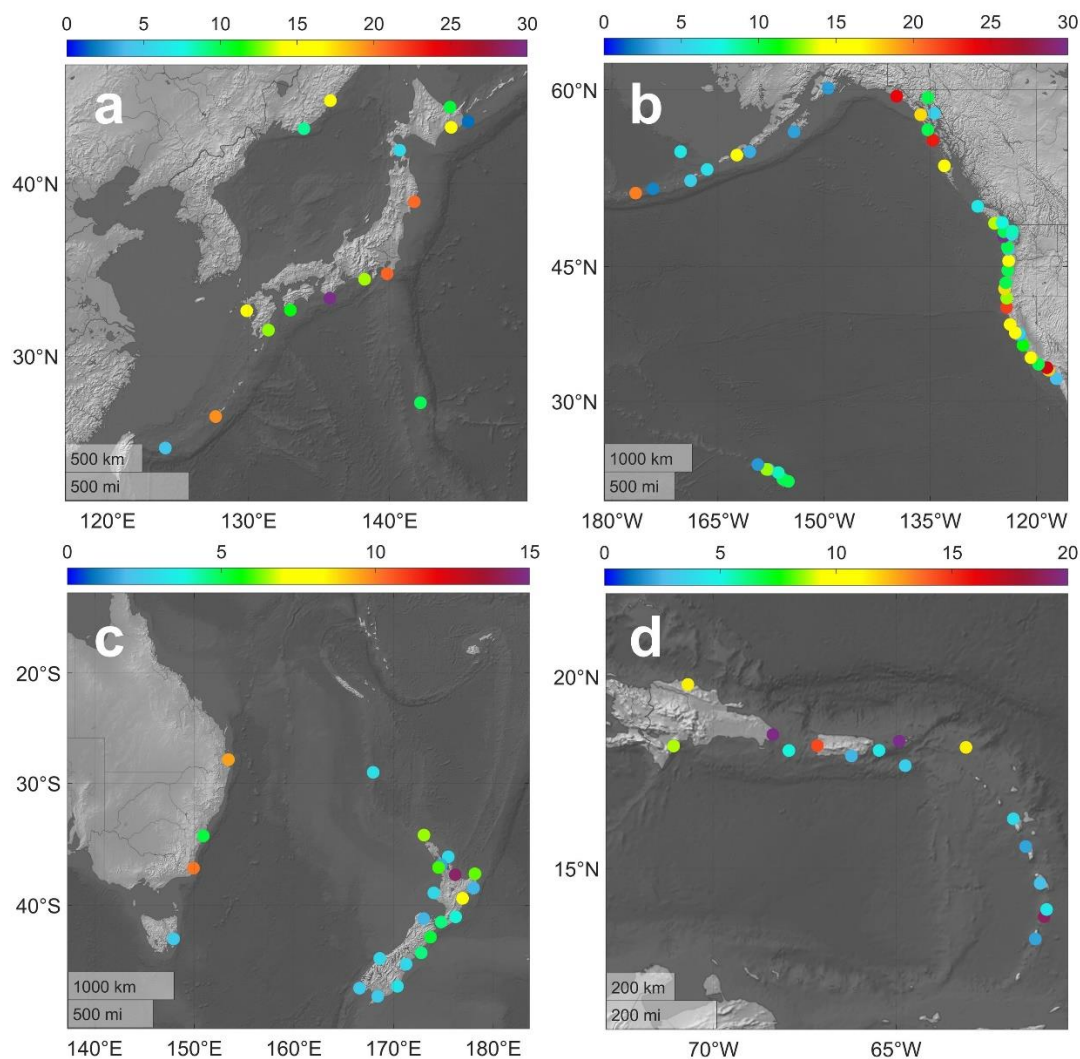
430

Figure 8. Amplification, β in: (a) Japan; (b) the Northeast Pacific; (c) New Zealand and Australia; and (d) the Caribbean. Note diverse color scales. Map backgrounds made in MATLAB using Natural Earth (naturalearthdata.com).

435

5. Discussions and Conclusions

Analyses of high-resolution WL data from tide gauges (with local P_A, where possible) provides an unprecedented global view of a combined air-shock/oceanic tsunami, the Tonga Event. A moderate oceanic tsunami was measurable at

440 nearly all Pacific Ocean tide gauges and deep-water buoys, but at only a few stations elsewhere. In addition, most tide gauges and about half of the deep-water buoys also observed the air-shock tsunami. In the North Pacific, wave amplitudes and energy were comparable to the Chilean Event.

Out of 308 tide gauges, 10 showed an air-shock amplification of > 20, 54 were > 10x, 113 were >5x, 204 were 2x or more, and 230 were 2 or less; the remainder did not register any air-shock signal. Hence, the possibility of significant
445 amplification is a relatively rare, but potentially locally important, process. We note that much of the world's coastline is still not gauged, and there are likely locations in which the air-shock tsunami was amplified, but not measured. Thus, the Tonga Event tsunami was "global" because of the reach of the air-shock and its impacts on WLs. There are several conclusions regarding the air-shock tsunami:

- It arrived before the oceanic wave at all stations where both were observed, though the oceanic wave was larger
450 at stations where both occurred.

- The air-shock transited the globe multiple times; on every pass it imparted additional energy to WL fluctuations, leading to a ~25% longer decay timescale than for recent oceanic tsunamis generated by earthquakes.

- The re-focusing of the air-shock near the antipode of the eruption may have increased nearby tsunami
455 amplitudes in Africa and the Mediterranean. The reasons for the strong Caribbean response are unclear.

- The first wave observed at deep-water pressure gauges was the super-critical air-shock forced wave predicted by theory, but at most tide gauges only the sub-critical free wave response was observed.

- The nominal amplification, a_n, shows that deep water allows strong growth of the forced wave beneath an air-shock (Proudman resonance). The large total amplification, β, at Japanese coastal stations suggest that deep
460 water trenches around the Pacific "Ring-of-Fire" (with its many volcanoes) and elsewhere may increase the potential for large air-shock tsunamis.

What lessons can we learn from this air-shock tsunami regarding future hazards? The Tonga Event drove air-shock tsunamis no larger in the far field than ~210mm based on air-shocks of ~0.5 to 5 mb. However, the total amplification, β,
465 varied from ~1 to 35X. Such large values were mainly seen at coastal locations; island locations typically had $\beta < 5$, with a few exceptions (e.g., Hawai'i and Naha). We conceptualize the situation with an ocean trench between the source and the coastal station in Figure 9; this is typical for much of the Pacific "Ring-of-Fire". With deep-water resonance and coastal processes, an amplification of up to $\beta = 36$ is plausible, in which case an initially modest (5mb) P_A-spike can become a ~1.8m tsunami.

470 The air-shock from the Tonga event was small, but β was >10 in many parts of the world with active volcanoes, including Italy, Alaska, Japan, and New Zealand. A much larger air-shock can occur close to a VEI 6-7 volcanic explosion. In 1883, ship barometers measured fluctuations of 1-2 inches of mercury (30-60mb) near Krakatoa (Symons, 1888). Taking

30mb as a conservative upper limit for a VEI 6 event and β = 10 to 35, an air-shock tsunami of 3.5 to ~10m is possible. In most cases, this would be later followed by larger water waves, but the rapid arrival of air-shock waves of this size could be

475   catastrophic and might occur in some locations without being followed by an oceanic tsunami. Present-day warning systems are designed for oceanic tsunamis, and do not generate timely warnings for an air-shock event. Hence, a reconsideration of air-shock tsunamis from explosive eruptions similar to Krakatoa would be timely. The reasons why certain regions exhibited a larger amplification (e.g., β) than others, and the possible role of bathymetry, remains to be understood, e.g., through modeling.
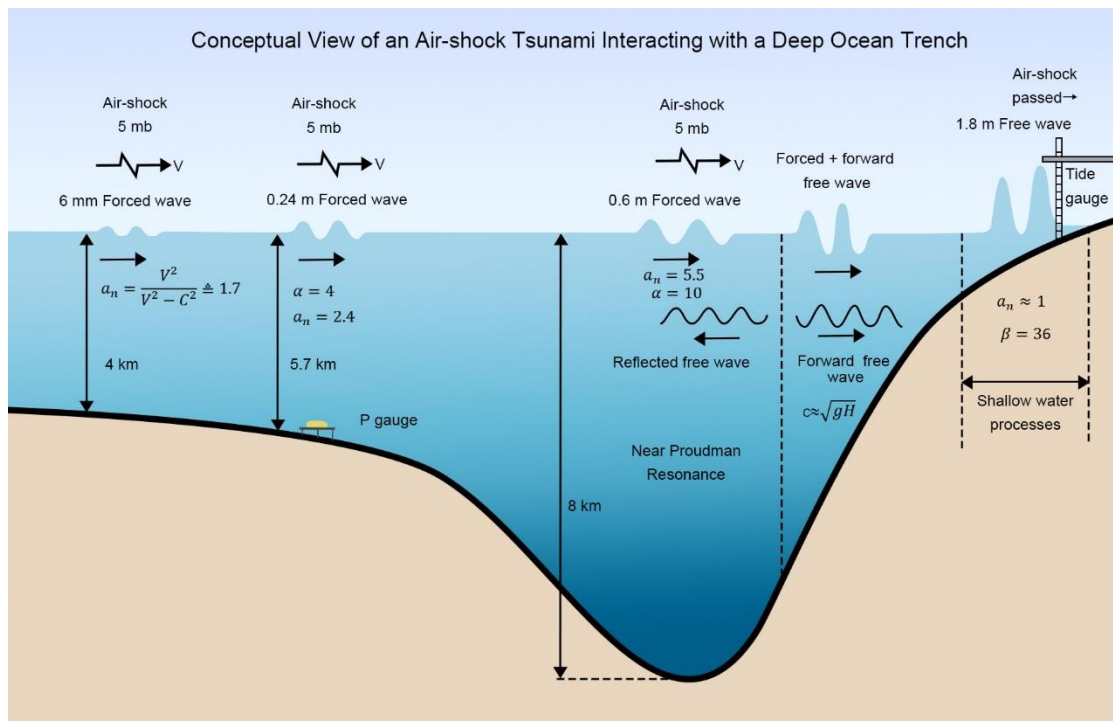
480

Figure 9. Conceptual view of amplification of an air-shock tsunami, based on Tonga-Event observations. An air-shock of 5mb is amplified by Proudman resonance in the trench, and again by shallow water processes, after reflection of a free wave

485   by the steep topography landward of the trench. With β = 36, a 1.8m tsunami occurs at the tide gauge. A larger air-shock would lead to a proportionally larger response.

490

22

Appendix A: Extended Details of Materials and Methods

A1. Data Inventory

495   We acquired one-minute resolution data from the following sources: the European Commission (EC) World Sea Levels Database (https://webcritech.jrc.ec.europa.eu/SeaLevelsDb/Home), the Intergovernmental Oceanographic Commission (IOC) sea level station monitoring facility (https://www.ioc-sealevelmonitoring.org/; VLIZ, 2022), the National Oceanic and Atmospheric Administration (NOAA) CO-OPS Tides and Currents tsunami warning network (https://tidesandcurrents.noaa.gov/tsunami/), and Land Information New Zealand (https://www.linz.govt.nz/sea/tides/sea-

500   level-data/sea-level-data-downloads), plus data obtained by direct communication from the National Institute of Water and Atmospheric Research (NIWA) of New Zealand (https://niwa.co.nz/our-services/online-services/sea-levels). Other stations from these networks with less frequent data were used when 1-min data were not available. Tidal predictions and residuals are provided in the EC and NOAA databases, however, a tidal signature or a slope sometimes remains in the provided residuals, and the IOC and NIWA data does not provide any predictions. Therefore, we apply an EEMD analysis (Huang et

505   al., 1998) to all WL data to remove low frequency components and biases in mean water level to yield data in which the tsunami signal is dominant.

Air pressure (P_A) records at 1-minute resolution is downloaded from the Chilean Meteorological Directorate (CMD; https://climatologia.meteochile.gob.cl/), the Australia Bureau of Meteorology (BOM; http://www.bom.gov.au/climate/data/), and the Instituto Superiore per la Protezione e la Ricerca Ambientale (ISPRA; https://www.mareografico.it/) network for

510   Mediterranean locations, 6min P_A data is downloaded from NOAA at tide gauges and P_B data from offshore buoys in the Pacific and Caribbean (https://tidesandcurrents.noaa.gov/stations.html?type=Meteorological+Observations; https://www.ndbc.noaa.gov/obs.shtml), and 10-min P_A data is acquired from the Japan Meteorological Agency (JMA; https://www.data.jma.go.jp/obd/stats/etrn/index.php) and the National Institute of Water and Atmospheric Research National Climate Database (NIWA/NCD; https://cliflo.niwa.co.nz/). A total of 137 air pressure locations were used, listed in Table

515   S5.

Finally, we download data from 30 Pacific deep-water buoys (see Table S1) from the National Data Buoy Center (NDBC; https://www.ndbc.noaa.gov/obs.shtml) tsunami warning center operated by NOAA; these provide 1-min data during "active" WL events and 15-min data otherwise. Other buoys were investigated, but because the buoys only sometimes operated at 1-min resolution, many were not triggered until the air-shock was past; thus, the air shock wave was most often

520   not captured. All buoy data and air pressure data were conditioned using EEMD as described above.

A2. Water Level (WL) Analysis

23

Air-shock magnitudes and arrival times, and the amplitudes of the largest positive and negative tsunami waves at each location are determined from the WL residuals via numerical and visual estimation of the residual time series. The "first arrival" times and amplitudes represent the effects of the air-shock wave, which travels faster than the oceanic tsunami; times are determined by finding the rising edge of the first obvious anomalous wave in the residual WL time series, and the air-shock amplitude is defined as the maximum WL immediately after the first arrival (Table S3). At a small number of locations, the air-shock wave could not be clearly observed, as noted in Table S3, and in Figs. 1(c),(d). We compare the distances and first arrival times at all tide gauges stations via robust regression (Holland and Welsch, 1977) and find an estimate of the air-shock velocity from the slope of the regression as 1054 ± 7km hr^{-1} (Figure S11(b)), slightly less than that estimated from the air pressure gauges (1115 ± 3 km hr^{-1}; Figure S11(a)). These estimates can be compared to the much slower celerity estimate for the water wave component of the tsunami (708 ± 8 km hr^{-1}; Figure S11(c)), clearly demonstrating that the "first arrival" WLs are due to the air-shock. Note that the water-wave celerity corresponds to an average water depth of about 5km.

The timings and amplitudes of the largest positive (negative) waves due to the oceanic tsunami are determined by when the first local maximum (minimum) occurs after the first arrival of the tsunami. At some locations, slightly larger amplitudes are seen many hours later, usually on the following tidal cycle (i.e., "tidal pulsing"). WLs and times for maximum WLs, as well as the differences between extreme levels and the air-shock arrival are given in Table S2 and Fig. 1(a),(c) and Figure S5 and S6, and the same parameters for minimum WL are provided in Table S4 and Figures S7 and S8. The time differences between "first arrival" and max/min WLs are shown in Figures S9 and S10. Determination of air-shock ("P_A-spike") amplitudes was carried out in the same manner as for the tsunami amplitudes.

A3. Air-pressure gauge choices for Kushimoto

Comparison of the Kushimoto tide gauge WLs to offshore buoy #21420 and air pressure (Figure 3) raises the difficulty that there is no P_A station within more than 300km of the buoy; we use, therefore, the two nearest. Aburatsu (~465 km) is on a direct line from Tonga and the buoy, while Kushimoto is 305 km from the circle centered on Tonga through the buoy. Accounting for the distance between the coastal gauges and the buoy using a shockwave velocity of 1092 km hr^{-1} (Table S3), we shift the time index of the P_A records by 16 and 26 minutes, respectively. Both P_A records are used, because the sparse, 10 min, resolution of the P_A records precludes either from completely capturing the air-shock.

A4. Energy Decay Analysis

Following (Rabinovich, 1997), we detide 1-min NOAA WL data, remove any residual trend, and then produce power spectra for 6hr segments of the WL residual, with an overlap of 3 hours between successive analyses. A multi-tapered method (McCoy et al., 1998) was applied, because it reduces noise and edge effects, but still conserves energy. The energy

within the tsunami band (between 10 minutes and 3 hours) was then integrated for each 6hr period and an exponential decay

model of form $E = E_o e^{\frac{-t}{t_d}}$ applied, where E_o is the peak energy in the fit and t_d is the e-folding (decay) time scale. To

account for the initial "diffusion period" (Van Dorn, 1984; 1987), the two initial, largest energy values were removed; hence,

555   E_o represents the energy at the commencement of exponential decay. The exponential decay was fit to all tsunami-band

energy values until measurements dipped below the noise floor. The noise floor was defined as the 80% percentile energy in

the tsunami band from 7-12 days after the event. Each fit was examined for validity, and the range of points in the fit was

manually adjusted in five cases. For fits for which the standard error in the coefficients was more than 20%, the coefficient

value was removed. The analysis was applied to four events: The 2009 Samoa tsunami, the 2010 Chilean tsunami, the 2011

560   Tohoku tsunami, and the 2022 Tonga tsunami. However, due to the low energy in the Samoa event, we focus primarily on

the other three. In our analysis, we also distinguish between coastal and island stations. Unfortunately, high resolution

DART data are not presently available over a sufficiently long time scale to repeat the analysis of (Rabinovich et al., 2013)

exactly.

A5. Uncertainty and Errors

565   The possible sources of uncertainty in this study arise from:

1) <u>Instrumental accuracy:</u> Measurements of WL at most locations considered report values to an accuracy of 1mm, and US

locations from the NOAA tsunami network are only reported to an accuracy of 10mm. Values are reported to this accuracy

in figures and tables. However, due to oceanographic noise from coastal waves and other processes, a "noise floor" of at

least 10 mm is likely at all locations. Thus, we assume all locations have an uncertainty of ±10mm in the calculations of β

570   below. This noise level represents a small uncertainty in the determination of maximum and minimum tsunami heights, e.g.,

a 1000mm tsunami wave would have a relative error of 1%. However, there will be a larger relative error in the estimation of

the air-shock WL amplitude, e.g., a 20-200mm air-shock WL would have a relative error of 5 to 50%. All P_A readings are

reported to an accuracy of 0.1mb. Since the P_A fluctuations are mainly in a range of 0.5 to 2.0mb, the instrumental error may

be up to 20%.

575   2) <u>Mean offset/bias in residuals:</u> Common estimates for tidal prediction, such as those performed in the downloaded residual

products here, subtract tidal components from water levels using harmonic analysis methods, which are typically based on

past epochs and may not always remove all tide-related fluctuations or may include a bias due to sea-level rise or other

oceanographic processes (Jay, 2009; Zaron and Jay, 2014; Devlin et al., 2014; Devlin et al., 2017; Devlin et al., 2021; Fang

et al., 1999). These artifacts may give erroneous estimates of tsunami-related WLs. Our application of EEMD to further

580   separate and remove leftover tidal components in the lower modes of the decomposition largely alleviates this issue.

Analyses of the mean values of residuals WLs after the EEMD conditioning show that almost all residual time series have a

mean value $\ll$ 10mm, a problem no larger than the instrumental accuracy issue. However, we still subtract the mean bias

from our reported results of WL (max/min tsunami waves and air-shock amplitudes). Similarly, the EEMD process also removes diurnal and low-frequency variability in P_A, and analyses of the residuals show that all locations have mean values less than 0.001mb. Thus, the offset or bias in P_A values is insignificant in relation to the instrumental accuracy.

3) <u>Coarse temporal resolution:</u> Nearly all WL data used here are 1-min resolution. This is sufficient in the estimation of the oceanic and air-shock related waves, which have frequencies of ~5 min to a few hours. However, only some of our P_A data is at 1-min resolution (Italy, Chile, and Australia), the remainder is 6-min resolution (US) or 10-min resolution (NZ and Japan). The pressure wave is a rapidly changing phenomenon which shifts from strongly positive to strongly negative over a short time (20-60 min) Therefore, it is possible that the P_A spikes may not be fully captured in the coarser resolution data and may misrepresent the actual intensity of the air-shock wave. This unavoidable problem is the largest source of uncertainty in our study. We account for this by qualitatively increasing the uncertainty values of the instrumental accuracy for P_A ($\pm$0.1mb) to $\pm$0.15mb for the 6-min data and $\pm$0.2mb for the 10-min data.

The calculation of β divides the air-shock induced WL by the P_A spike; i.e., $\beta = \frac{WL_{airshock}}{P_A}$. We determine the relative error in β by propagating the uncertainties detailed above as: $\frac{\delta\beta}{\beta} = \sqrt{\left(\frac{\delta WL}{WL}\right)^2 + \left(\frac{\delta P_A}{P_A}\right)^2}$; δWL is 10 mm, δP_A is 0.1mb at 1-min stations, 0.15mb at 6-min stations, and 0.2mb at 10-min stations. Using these error estimates, 21 locations have relative uncertainties in β which are greater than 50%, four of which are greater than 100% (statistically insignificant). The overall average uncertainty is 30.8%. Best results were found for 1-min pressure data (e.g., Chile had an average of 16% and Australia had an average of 13%), and somewhat less accurate results for 10-min pressure data (e.g., Japan and New Zealand both have averages of 27%). However, the largest uncertainties occurred in places where air-shock amplitudes were very small, regardless of air pressure data resolution.

605   **Code and Data Availability** All data used in this study are deposited in an online repository of the Harvard Dataverse at: https://doi.org/10.7910/DVN/F0G63H. Datasets included are original 1-min water levels, post-EEMD water level residuals, original air pressure data (1-minute, 6-minute, and 10-minute resolution), and post-EEMD air pressure residuals. All code was performed in MATLAB and can be shared via direct communication with the authors.

610   **Video Supplement** Four short movies are also provided and uploaded separately; movie captions are provided in the Supplement.

Author Contributions: All authors contributed to conceptualization, validation, visualization, and reviewing/editing. A.T.D. contributed data curation, formal analysis, investigation, methodology, software, and original draft writing. D.A.J.
615   contributed formal analysis, investigation, methodology, and original draft writing. S.A.T. contributed formal analysis, investigation, software, and methodology. J.P contributed funding acquisition and supervision.

Competing Interest Statement: The authors have no competing interests.

References

630   Adam, D.: Tonga volcano eruption created puzzling ripples in Earth's atmosphere, Nature 601, 497 2022.

Amores, A., Monserrat, S., Marcos, M., Argüeso, D., Villalonga, J., Jordà, G., and Gomis, D.: Numerical Simulation of Atmospheric Lamb Waves Generated by the 2022 Hunga-Tonga Volcanic Eruption, Geophysical Research Letters, 49(6), e2022GL098240, https://doi.org/10.1029/2022GL098240, 2022.

Devlin, A. T., Jay, D. A., Talke, S. A., and Zaron, E.: Can tidal perturbations associated with sea level variations in the
635   western Pacific Ocean be used to understand future effects of tidal evolution?, Ocean Dynamics, 64(8), 1093-1120, https://doi.org/10.1007/s10236-014-0741-6, 2014.

Devlin, A. T., Pan, J., and Lin, H.: Extended Water Level Trends at Long-Record Tide Gauges Via Moving Window Averaging and Implications for Future Coastal Flooding, Journal of Geophysical Research: Oceans, 126(10), e2021JC017730, https://doi.org/10.1029/2021JC017730, 2021.

640   Devlin, A. T., Jay, D. A., Talke, S. A., Zaron, E. D., Pan, J., and Lin, H.: Coupling of sea level and tidal range changes, with implications for future water levels, Scientific reports, 7(1), 1-12, https://doi.org/10.1038/s41598-017-17056-z, 2017.

Fang, G., Kwok, Y. K., Yu, K., and Zhu, Y.: Numerical simulation of principal tidal constituents in the South China Sea, Gulf of Tonkin and Gulf of Thailand, Continental Shelf Research, 19(7), 845-869, https://doi.org/10.1016/S0278-
645   4343(99)00002-3, 1999.

Garret, C. J. R.: A theory of the Krakatoa tide-gauge disturbances, Tellus, 22(1), 43–52, https://doi.org/10.1111/j.2153-3490.1970.tb01935.x, 1976.

Green, G.: On the motion of waves in a variable canal of small depth and width, Transactions of the Cambridge Philosophical Society, 6, 457, bibcode: 1838TCaPS...6..457G, 1838.

650   Holland, P. W., and Welsch, R. E.: Robust regression using iteratively reweighted least-squares, Communications in Statistics-theory and Methods, 6(9), 813-827, https://doi.org/10.1080/03610927708827533, 1977.

Huang, N. E., Shen, Z., Long, S. R., Wu, M. C., Shih, H. H., Zheng, Q., Yen, N. C., Tung, C. C., and Liu, H. H.: The empirical mode decomposition and the Hilbert spectrum for nonlinear and non-stationary time series analysis, Proceedings of the Royal Society of London, Series A: mathematical, physical and engineering sciences, 454(1971),
655   903-995, https://doi.org/10.1098/rspa.1998.0193, 1998.

Jay, D. A.: Evolution of tidal amplitudes in the eastern Pacific Ocean, Geophys. Res. Lett., 36(4), L04603, https://doi.org/10.1029/2008GL036185, 2009.

Kubota, T., Saito, T., and Nishida, K.: Global fast-traveling tsunamis driven by atmospheric Lamb waves on the 2022 Tonga eruption, Science, 377(6601), 91-94, https://doi.org/10.1126/science.abo4364, 2022.

660   Lamb, H., 1911: On atmospheric oscillations. *Proc. Roy. Soc.*, **A84**, 551–572, https://doi.org/10.1098/rspa.1911.0008.

Levin, B. W. and Nosov, M.: Physics of tsunamis, Edi. 2, Vol. 327, Springer, Switzerland, https://doi.org/10.1007/978-3-319-24037-4, 2009.

Lilly, J. M.: Element analysis: a wavelet-based method for analysing time-localized events in noisy time series,
665   Proceedings of the Royal Society A: Mathematical, Physical and Engineering Sciences, 473(2200), 20160776, https://doi.org/10.1098/rspa.2016.0776, 2017.

McCoy, E. J., Walden, A. T., and Percival, D. B.: Multitaper spectral estimation of power law processes, IEEE Transactions on Signal Processing, 46(3), 655-668, doi: 10.1109/78.661333, 1998.

Mori, N., Takahashi, T., Yasuda, T., and Yanagisawa, H.: Survey of 2011 Tohoku earthquake tsunami inundation and run-
670   up, Geophysical Research Letters, 38(7), L00G14, https://doi.org/10.1029/2011GL049210, 2011.

Olabarrieta, M., Valle-Levinson, A., Martinez, C. J., Pattiaratchi, C., and Shi, L.: Meteotsunamis in the northeastern Gulf of Mexico and their possible link to El Niño Southern Oscillation, Natural Hazards, 88(3), 1325-1346, https://doi.org/10.1007/s11069-017-2922-3, 2017.

Pattiaratchi, C. B. and Wijeratne, E. M. S.: Are meteotsunamis an underrated hazard?, Philosophical Transactions of the
675   Royal Society A: Mathematical, Physical and Engineering Sciences, 373(2053), 20140377, https://doi.org/10.1098/rsta.2014.0377, 2015.

Pelinovsky, E. Talipova, T., Kurkin, A., and Kharif, C.: Nonlinear mechanism of tsunami wave generation by atmospheric disturbances, Natural Hazards Earth Syst. Sci, 1(4), 243–250, https://doi.org/10.5194/nhess-1-243-2001, 2001.

Pekeris, C.L.: Atmospheric oscillations. *Proc. Roy. Soc*. **A158**, 650-671, 1937.
680 Pekeris, C.L.: Propagation of a pulse in the atmosphere. *Proc. Roy. Soc*. **A171**, 434-
449, 1939.

Press, F.: Volcanoes, Ice and Destructive Waves. Engineering and Science, 20(2), 26-29, 1956.

Rabinovich, A.B.: Spectral analysis of tsunami waves: Separation of source and topography effects, Journal of Geophysical Research: Oceans, 102(C6), 12663-12676, https://doi.org/10.1029/97JC00479, 1997.

685 Rabinovich, A. B., Candella, R. N., and Thomson, R. E., The open ocean energy decay of three recent trans-Pacific tsunamis, Geophysical Research Letters, 40(12), 3157-3162, https://doi.org/10.1002/grl.50625, 2013.

Rioul, O. and Vetterli, M.: Wavelets and signal processing, IEEE Signal Processing Magazine 8(4), 14–38, doi: 10.1109/79.91217, 1991.

Šepić, J. and Rabinovich, A. B.: Meteotsunami in the Great Lakes and on the Atlantic coast of the United States generated
690   by the "derecho" of June 29–30, 2012 in: Meteorological Tsunamis: The US East Coast and Other Coastal Regions, Springer, 75-107, DOI: 10.1007/978-3-319-12712-5_5, 2014.

Šepić, J., Vilibić, I., Rabinovich, A. B., and Monserrat, S.: Widespread tsunami-like waves of 23-27 June in the Mediterranean and Black Seas generated by high-altitude atmospheric forcing, Scientific Reports, 5(11682), 1-8, https://doi.org/10.1038/srep11682, 2015.

695 Shufeldt, R. W., Comments regarding correspondent "S" in Science No 63., Science 3, No 65, 531-532, 1885.

Symons, G. (Ed.): The eruption of Krakatoa and subsequent phenomena, Trubner & Co., London, 1888.

Titov, V., Rabinovich, A. B., Mofjeld, H. O., Thomson, R. E., and González, F.I.: The global reach of the 26 December 2004 Sumatra tsunami, Science, 309(5743), 2045-2048, https://doi.org/10.1126/science.1114576, 2005.

Torrence, C., and Compo, G. P., A practical guide to wavelet analysis, Bull. Am. Meteorol. Soc., 79(1), 61–78,
700   https://doi.org/10.1175/1520

Van Dorn, W. G.: Some tsunami characteristics deducible from tide records, Journal of Physical Oceanography, 14(2), 353-363, https://doi.org/10.1175/1520-0485(1984)014%3C0353:STCDFT%3E2.0.CO;2, 1984.

Van Dorn, W. G.: Tide gage response to tsunamis. Part II: Other oceans and smaller seas. Journal of Physical Oceanography, 17(9), 1507-1516, https://doi.org/10.1175/1520-0485(1987)017%3C1507:TGRTTP%3E2.0.CO;2,
705   1987.

Watanabe, S., Hamilton, K., Sakazaki, T., and Nakano, M:. First Detection of the Pekeris Internal Global Atmospheric Resonance: Evidence from the 2022 Tonga Eruption and from Global Reanalysis Data, Journal of the American Meteorological Society, (early release) https://doi.org/10.1175/JAS-D-22-0078.1, 2022.

Wharton, N. J. L.: On the seismic sea waves caused by the eruption of Krakatoa, August 26th and 27th, 1883 in: The
710   eruption of Krakatoa and subsequent phenomena, edited by Symons, G., Trubner & Co., London, 89-151, 1888.

Williams, D. A., Horsburgh, K. J., Schultz, D. M., and Hughes, C. W.: Proudman resonance with tides, bathymetry and variable atmospheric forcings, Natural Hazards 106(2), 1169–1194, https://doi.org/10.1007/s11069-020-03896-y, 2021.

Witze, A.: Why the Tonga eruption will go down in the history of volcanology, Nature, 602(7897), 376-378, 2022.

715 Zaron, E.D. and Jay, D. A.: An analysis of secular change in tides at open-ocean sites in the Pacific, Journal of Physical Oceanography, 44(7), 1704-1726, https://doi.org/10.1175/JPO-D-13-0266.1, 2014.